Faraday Discussions

Cite this: *Faraday Discuss.*, 2022, **239**, 219

ROYAL SOCIETY OF CHEMISTRY

PAPER

View Article Online
View Journal | View Issue

Zinc germanium nitrides and oxide nitrides: the influence of oxygen on electronic and structural properties†

Joachim Breternitz *[a] and Susan Schorr *[ab]

Received 14th February 2022, Accepted 25th March 2022
DOI: 10.1039/d2fd00041e

Zinc containing ternary nitrides, in particular $ZnSnN_2$ and $ZnGeN_2$, have great potential as earth-abundant and low toxicity light-absorbing materials. The incorporation of oxygen in this system – may it be intentional or unintentional – affects the crystal structure of the materials as well as their optical band gaps. Herein, we explore the origins of structural changes between the wurtzite type and its hettotype, the β-$NaFeO_2$ type, and highlight the effect of oxygen. Furthermore, we study the electronic structure and bonding in order to understand the reason for the narrower band gap of zinc germanium oxide nitrides as opposed to pure zinc germanium nitride.

Introduction

Solar cells are the most direct way to transform the energy from the sun, our largest energy reservoir, into immediately useable electrical energy. The development of solar cells has made big steps and solar energy is currently the cheapest form of energy available,[1] mostly relying on Si wafer-based solar cells. However, silicon has some drawbacks, most prominently its indirect band gap. This affords the use of relatively thick layers of Si to achieve a good absorption of light and, hence, makes Si solar cell devices inflexible and heavy. While this is not a major problem for landside or domestic installations, other applications, such as mobile devices and aviation, need a highly efficient power supply that is also lightweight and thin. For this, alternative technologies have emerged, with CdTe having reached the commercialisation phase.[2] However, many of these alternative photovoltaic absorber materials like CdTe,[2–7] (In, Ga)Pn (Pn = N, P, As),[8–17] Cu(In, Ga)S_2 [18–21] or lead halide perovskites[22–25] suffer from the inclusion of extremely scarce or toxic elements. Te (0.001 ppm), Cd (0.13 ppm), In (0.25 ppm – all by

[a]*Helmholtz-Zentrum Berlin für Materialien und Energie GmbH, Structure and Dynamics of Energy Materials, Hahn-Meitner-Platz 1, 14109 Berlin, Germany. E-mail: joachim.breternitz@helmholtz-berlin.de; susan.schorr@helmholtz-berlin.de*

[b]*Department Geosciences, Freie Universität Berlin, Malteserstraße 74-100, 12249 Berlin, Germany*

† Electronic supplementary information (ESI) available: Supplementary DOS and COHP plots. Input files for the calculations are available *via* Zenodo DOI: 10.5281/zenodo.6066232. See DOI: 10.1039/d2fd00041e

weight)[26] are some of the very scarce elements that would prevent a global scale application of such materials.[18] Moreover, Cd and Pb are very toxic elements, the use of which is banned in the European Union and many other countries.[27]

Given these limitations, there is a strong drive to develop truly sustainable solar cell materials that combine the advantages of thin film solar cells with the use of non-toxic and earth abundant materials, therefore allowing for cheap and efficient solar cell devices. A viable strategy in the past has been the replacement of problematic elements by less toxic and more abundant alternatives, like the development of lead-free halide perovskite solar cells based on Sn^{2+}.[28–30] The downside of this approach is, however, that the choice of alternative elements is severely reduced as they need to show chemical and structural similarity – *i.e.* to replace Pb^{2+}, one needs an element that readily forms divalent cations and has a similar coordination environment as otherwise a different phase with completely different properties may be preferable. $CH_3NH_3NiI_3$ containing Ni^{2+}, for instance, is reported to crystallise in a non-perovskite phase.[31]

To enlarge the window for replacing problematic elements, substituting ions with more than one species is possible. Replacing Pb^{2+} with equimolar amounts of Ag^+ and In^{3+}, for instance, has led us to the experimental discovery of $Cs_2AgInBr_6$.[32] Applying the same concept to In^{3+} in InN would lead to the use of equimolar divalent and tetravalent cations, such as Zn^{2+} and Sn^{4+}.[33–36] This approach has been shown to work and $ZnSnN_2$ was identified as a potential photovoltaic absorber material with reported experimental band gaps anywhere between 1–2.4 eV.[36] While there have been some proof-of-concept reports for photovoltaic devices using $ZnSnN_2$,[35,37,38] the range of reported optical band gaps for nominally the same material may sound surprising at first. However, two main explanations have been discussed for this behaviour: (a) the inclusion of oxygen in the material[39,40] and (b) a cation order–disorder mechanism that tunes the band gap.[41,42] Both effects often occur intertwined and it is therefore necessary to briefly discuss the second one in the next section in order to understand the first. While the work on $ZnSnN_2$ has largely relied on computational results, many more experimental studies have been performed on the lighter analogue $ZnGeN_2$. The latter has a distinctly larger band gap in the range of 3.2 eV,[43] but it has the advantage that its stability is larger due to a more negative formation energy.[44] Therefore, the study of this material as a model system that is easier to study allows us to understand the phenomena in these ternary nitride compounds. Before moving to the focus on photovoltaics, $ZnGeN_2$ and the oxide nitride materials $Zn_{1+\nu}GeN_2O_\nu$ have been studied extensively as photocatalysts for water splitting reactions.[45–50] From a chemical point-of-view, these oxide nitride materials have been rationalised as the intermixing of $ZnGeN_2$ and ZnO.[45,51,52] We have shown recently in a systematic study that the overall ammonolysis reaction of Zn_2GeO_4 – commonly the synthesis route for these compounds – indeed proceeds in this way.[51] It needs to be emphasised, however, that this does not mean that $ZnGeN_2$ and ZnO are mixed on a macroscopic level or form domains in some way. Instead, this is not more than a mathematical decomposition of the oxide nitride composition. Instead of the above-mentioned formula $Zn_{1+\nu}GeN_2O_\nu$, we will use $Zn_{1+x}Ge_{1-x}(N_{1-x}O_x)_2$ – a simple transformation, which emphasises on an equal number of cations and anions and retains the overall ratio of cations and anions throughout the series.[51,53] Oxide nitrides have been reported to exhibit a smaller optical band gap of $\approx$2.7 eV as compared to that of pure $ZnGeN_2$, but recent

studies have suggested that this is particularly true for oxygen rich oxide nitrides, while oxygen poor compounds tend to have an optical band gap much closer to the 3.2 eV of pure $ZnGeN_2$.[51] This reduction has been explained as an effect of p–d orbital repulsion between the Zn(3d) and the N(2p) and O(2p) states at the valence band maximum.[45,54] While p–d repulsion should, in principle, exist for pure nitrides and oxide nitrides, we aim to understand the contribution of oxygen in these oxide nitrides more thoroughly and to understand the bonding that causes the band gap decrease in the oxide nitride system $Zn_{1+x}Ge_{1-x}(N_{1-x}O_x)_2$.

Crystal structures of $Zn_{1+x}Ge_{1-x}(N_{1-x}O_x)_2$

Two principal crystal structures have been reported for oxide nitride materials: the hexagonal wurtzite type, which was observed in oxygen rich compounds[55] and the orthorhombic β-$NaFeO_2$ type, which was observed in the oxygen poor cases.[53] This appears reasonable from a chemical point of view: ZnO crystallises in the wurtzite type structure, while $ZnGeN_2$ crystallises in the β-$NaFeO_2$ type structure.[56] Assuming those phases to be extreme cases in the system, it is only logical that there should be a transition from one crystal structure to the other. The reality is, however, more complex than this. There have also been experimental reports of nominally $ZnGeN_2$ in the wurtzite type crystal structure, which is a consequence of fully disordered cations in the system.[57] To understand this, it is important to briefly emphasise the relation of these two crystal structure types.

The hexagonal wurtzite type crystal structure in the space group $P6_3mc$ only has one crystallographic position for cations and one for anions (both on Wyckoff site 2b). This means that this structure type does not allow for any ordering of cations or anions and they are necessarily randomly distributed. This also means that the average bonding environment in the wurtzite type structure is equal, although Zn^{2+} (0.55 Å) and Ge^{4+} (0.39 Å) have considerably different ionic radii.[58] The β-$NaFeO_2$ type structure, on the other hand, is a hettotype of the wurtzite-type structure and crystallises in the orthorhombic subgroup $Pna2_1$.[59] The link is made through loss of symmetry elements, which in turns increases the degrees of freedom for the crystallographic sites and allows for the splitting of crystallographic positions. Instead of one distinct crystallographic site each for cations and anions, the β-$NaFeO_2$ type has two cation positions and two anion positions (all on the general 4a Wyckoff site). This means that, in principle, a compound with a 1 : 1 cation stoichiometry could attain fully ordered cations. In addition, these two crystallographic sites have the structural flexibility to accommodate different cation–anion bond lengths in the crystal structure.

From an experimental point-of-view, the transition from the wurtzite-type to the β-$NaFeO_2$ type can be observed in the appearance of supplementary reflections and the splitting of some peaks, which is due to the fact that the lattice constants no longer experience restrictions rendering them equal.‡ While the supplementary reflections are weak in X-ray diffraction and can easily be overlooked, the peak splitting is normally a much stronger hint for the β-$NaFeO_2$ type

‡ In fact, the lattice constants a and b in the orthorhombic β-$NaFeO_2$ type are not equal to each other in the case of total overlap, but rather have a ratio of $a/b = 2/\sqrt{3}$. This is due to the change of the crystal system from hexagonal to orthorhombic. We have discussed the crystallographic bases in more detail elsewhere.[59]

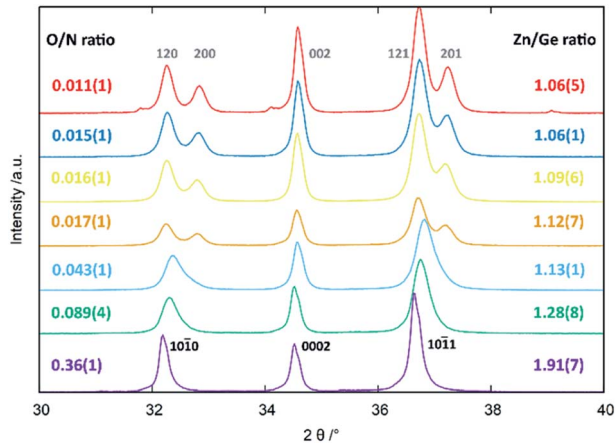

Fig. 1 Peak splitting in the region of 30–40° 2θ as a function of Zn/Ge and O/N ratios. The *hkil* indices according to the hexagonal wurtzite-type structure (black, bottom) and the *hkl* indices according to the orthorhombic β-$NaFeO_2$-type structure (grey, top) are given in the figure. Reprinted from ref. 51 with permission from the Royal Society of Chemistry. The original publication was published under the Creative Commons license CC BY 3.0.[60]

(Fig. 1). It needs noting, however, that this is only a necessary prerequisite in that *a* and *b* in the orthorhombic system can differ but do not have to. Therefore, very small deviations from the ideal hexagonal lattice will still be orthorhombic but may be so subtle that they cannot be detected with the experimental resolution. Therefore, when we speak of oxide nitrides as being of the wurtzite-type, this essentially means that we have no contradicting evidence for a hettotype structure. Nonetheless, our experimental data (Fig. 1) underlines the aforementioned trend that oxygen rich oxide nitrides crystallise in the wurtzite-type and the β-$NaFeO_2$ type is preferred for lower oxygen containing materials.

At this point, however, the complexity of ternary materials comes into play. With two crystallographic sites, order can occur, but this is not necessarily the case. While the fully ordered case (*i.e.* one distinct site for Zn^{2+} and one for Ge^{4+} exclusively) is energetically favoured, the energetic barrier against disorder is not large and it has been calculated that disorder affects the band gap strongly, with a decrease for disordered $ZnGeN_2$.[41,61–63] A fully disordered $ZnGeN_2$, however, would have a random cation distribution throughout the structure, indicative of the wurtzite-type. In between cation order and full disorder, different degrees of cation disorder are possible.[53] We have to distinguish between cation disorder caused by the off-stoichiometric composition of the material due to the oxygen content (Zn/Ge > 1), for which we use the term extrinsic disorder, and intrinsic disorder.[53] The latter is defined by Ge on Zn and Zn on Ge anti sites in equal amounts ($Ge^*_{Zn} = Zn^*_{Ge}$). Both disorder types can coexist in $Zn_{1+x}Ge_{1-x}(N_{1-x}O_x)_2$ and it is necessary to distinguish between them. Taking into account that the Zn on Ge anti sites (Zn_{Ge}) are caused by both extrinsic and intrinsic disorder, the difference $Zn_{Ge} - Ge^*_{Zn}$ would give a measure of the extrinsic disorder.

We recently uncovered that both disorder types exist simultaneously in zinc germanium oxide nitride, but both modes of disorder are independent of each

other.[53] The way intrinsic disorder affects the band gap has been thoroughly discussed, but the question remains how oxygen incorporation in the crystal structure affects the bonding and the band gap.

Sampled crystal structures in this study

We combine crystal structures experimentally obtained from Rietveld refinements of both neutron and X-ray data with DFT calculations. We have chosen three model structures for the DFT calculations in order to restrain the complexity of the system. Since our aim is to uncover the effect of oxygen incorporation, we have not introduced intrinsic disorder in the computational models. Fully ordered $ZnGeN_2$ is hence a rather straightforward choice to evaluate the fully ordered case. We chose not to use larger supercells for the modelling of oxygen induced disorder, but restricted ourselves to the 16-atom unit cell in the β-$NaFeO_2$ type in order to keep the positional restraints similar to those of the fully ordered case. Therefore, the composition $Zn_{1.25}Ge_{0.75}(N_{0.75}O_{0.25})_2$ was chosen and two different cases with the same composition but different arrangements were selected (Fig. 2). Case (a) consists of oxygen atoms that are as far away from each other as possible and with a coordination of 2 Zn atoms and 2 Ge atoms for one O atom and 3 Zn and 1 Ge for the other O atom – in line with the overall composition of the compound. Case (b), on the other hand, maximises the Zn–O bonding, as we determined earlier that crystal structures with a greater amount of Zn–O bonds tend to be more stable.[51] Both O atoms are surrounded by 3 Zn and 1 Ge. In addition, we compare these cases with three samples we studied experimentally

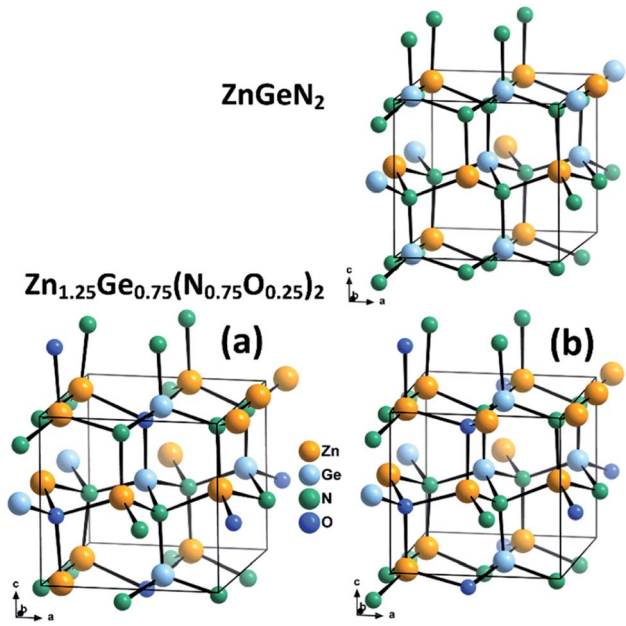

Fig. 2 Optimised crystal structures of $ZnGeN_2$ (top) and the two models of $Zn_{1.25}Ge_{0.75}(N_{0.75}O_{0.25})_2$ (bottom).

Table 1 Comparison of the lattice constants of the crystal structure of sample under investigation. A measure of the lattice distortion is given as α, with $\alpha = (b/2 - a/\sqrt{3})/(V/4)^{0.33}$ (a and b: orthorhombic lattice parameters; V: volume of the orthorhombic unit cell).[51] Ge^{*}_{Zn} is indicative of intrinsic disorder in the sample and the difference $Zn_{Ge} - Ge^{*}_{Zn}$ corresponds to the extrinsic disorder in the sample

Composition		A/Å	B/Å	C/Å	V/Å^3	A/%	Ge^{*}_{Zn}	$Zn_{Ge} - Ge^{*}_{Zn}$
$Zn_{1.04(1)}Ge_{0.96(1)}(N_{0.94(1)}O_{0.06(1)})_2$	Exp.	5.464(1)	6.443(1)	5.188(1)	182.62(1)	1.87(9)	0.01(2)	0.04(1)
$Zn_{1.05(1)}Ge_{0.95(1)}(N_{0.95(1)}O_{0.05(1)})_2$		5.487(1)	6.422(1)	5.192(1)	182.96(1)	1.21(9)	0.23(8)	0.05(1)
$Zn_{1.29(1)}Ge_{0.71(1)}(N_{0.71(1)}O_{0.29(1)})_2$		5.549(1)	6.427(1)	5.197(1)	185.35(1)	0.27(9)	0.24(6)	0.29(1)
$ZnGeN_2$	Calc.	5.50252	6.48303	5.24209	187.001	1.79	0	0
$Zn_{1.25}Ge_{0.75}(N_{0.75}O_{0.25})_2$ (A)		5.56905	6.54043	5.26973	191.945	1.51	0	0.25
$Zn_{1.25}Ge_{0.75}(N_{0.75}O_{0.25})_2$ (B)		5.54968	6.51646	5.26688	190.473	1.49	0	0.25

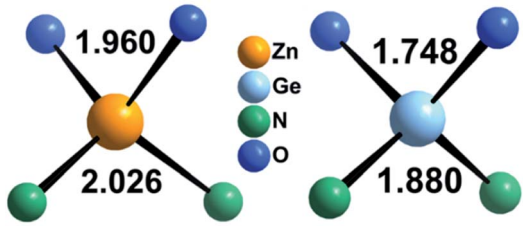

Fig. 3 Expected values for the bond lengths of Zn^{2+} and Ge^{4+} in tetrahedral coordination as derived from bond valence sums.[66]

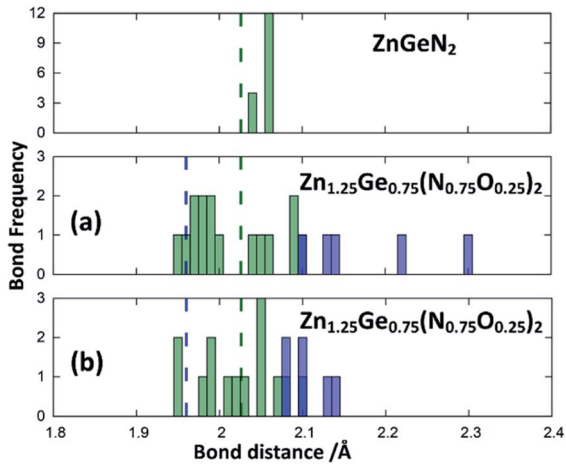

Fig. 4 Zn–N (green) and Zn–O (blue) distances from the structure optimisations of the crystal structures for $ZnGeN_2$ (top) and the two configurations of $Zn_{1.25}Ge_{0.75}(N_{0.75}O_{0.25})_2$, as depicted in Fig. 2. The expected distances from the bond valences are given as dashed lines.

using neutron diffraction to determine the levels of extrinsic and intrinsic disorder.[53]

The optimised crystal structures are slightly larger than the experimental ones, as expected for calculations using the PBE functional, but with volume deviations below 3% (Table 1). The deviation of the crystal structures from the ideal hexagonal setting, however, as expressed by α, is comparable to the highly ordered cases and significantly larger than for $Zn_{1.29(1)}Ge_{0.71(1)}(N_{0.71(1)}O_{0.29(1)})_2$, which contains both a large degree of intrinsic and extrinsic disorder. Furthermore, the oxygen rich oxide nitrides show a larger unit cell, which is consistent in computations and experiments. This hints that the volume increase is mainly caused by greater amounts of Zn and O, while the lattice parameter deviation is caused by disorder (intrinsic and extrinsic).

Bond valence analysis of $Zn_{1+x}Ge_{1-x}(N_{1-x}O_x)_2$

$Zn_{1.25}Ge_{0.75}(N_{0.75}O_{0.25})_2$ in configuration (b) is slightly more stable, with an energy difference of 122.6 meV/f.u. This is in line with our prior findings that Zn–O

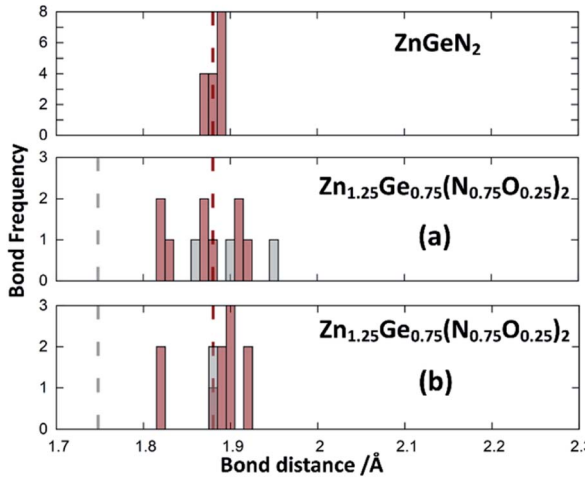

Fig. 5 Ge–N (red) and Ge–O (grey) distances from the structure optimisations of the crystal structures for $ZnGeN_2$ (top) and the two configurations of $Zn_{1.25}Ge_{0.75}(N_{0.75}O_{0.25})_2$ as depicted in Fig. 2. The expected distances from bond valences are given as dashed lines.

bonding appears to be preferred.[51] We will, however discuss both cases further, since the bonding situation is slightly different and can give some insight into the chemical nature of the bonding.

The bond valence concept mainly developed by Brown and O'Keeffe[64–67] solely uses atomic distances to determine the properties of chemical bonds and defines expected distances for atomic pairs in the defined chemical environment. This can be simply achieved by partitioning the valence (*i.e.* the charge) of the cations on the four bonds to the cations it is surrounded by. The expected values for the Zn–N and Zn–O distances are consistently longer than those for the Ge–N and Ge–O distances (Fig. 3). Taking the PBE related elongations into account, the Zn–N and Ge–N distances in the optimised structures are very consistent with the expected values from the bond valence model, but scatter relatively strongly (Fig. 4 and 5). The Zn–O and Ge–O distances, however, are consistently longer than the expected values.

This can be interpreted in a way that the energetic contribution of those bonds is lower than those of the Ge–N and Zn–N bonds. The same analysis is not directly possible for the experimentally derived crystal structures as the disorder for cations and anions restricts the distances to be the same. In those structures with strong cation ordering, however, the distances between the Zn site and its surrounding anions (1.99(2) Å < d_{Zn-X} < 2.07(2) Å) and the Ge site and its surrounding anions (1.85(1) Å < d_{Ge-X} < 1.93(1) Å) are distinctly different from each other and lie very much in the range of Zn–N and Ge–N bonds. The anisotropy between the different bond lengths is smaller for highly disordered experimental samples, in line with the decreasing lattice deviation in those samples. Although the oxide nitrides are generally more stable than pure nitrides, the comparably longer Zn–O and Ge–O bonds do not appear to stabilise zinc germanium oxide nitride.

Band gap and density of states

While the GGA treatment with the PBE functional along with Gaussian smearing to obtain the DOS leads to a serious underestimation of the absolute band gap size, its general trends are more reliable. The band gap energies extracted from the DOS are 1.5 eV for $ZnGeN_2$ and 0.4 eV for $Zn_{1.25}Ge_{0.75}(N_{0.75}O_{0.25})_2$. We note that this is very in line with the general trend of a decreasing band gap with increasing oxygen content.[43,51] Our calculations can therefore give an important hint as to how the introduction of oxygen in the system shifts the band gap levels. The conduction band minimum (CBM) is approximately equally contributed between the constituent elements, signifying that the contributing electronic states are probably largely degenerated. Furthermore, the shapes of the conduction band are largely similar for the pure nitride and the oxide nitrides, suggesting that the change of composition has little influence on it.

In a comprehensive theory by Wei and Zunger first derived for II–V semiconductor materials,[54] the reduction in the band gap energy is explained through p–d repulsion, *i.e.* an orbital overlap between the hybridised cation 4p states and anion 2p states with the cation 3d states, which leads to a further energy splitting and raises the antibonding orbitals that are situated at the top of the valence band. We have calculated the density of states (DOS) and projected DOS (pDOS) to verify which states form the valence band maximum (VBM). Indeed, the contributions at the VBM in the oxide nitride system are dominated by the Zn(3d), O(2p) and N(2p) contributions and a little Zn(3p) contribution (Fig. 6 and ESI†).

The same is true for $ZnGeN_2$, but with a general downwards shift of the states with respect to the Fermi level. This alone does, however, not allow a definitive answer as to whether the VBM increases or the conduction band minimum decreases. In order to gain a hint of this, we investigate the energy difference between the N(2s) and N(2p) band onsets on a specific N atom in the different structures. This can be done assuming that the N(2s) states are largely unaffected by any p–d repulsion and are not strongly influenced by the chemical environment as their contribution to bonding is small (Fig. 7). The energy difference

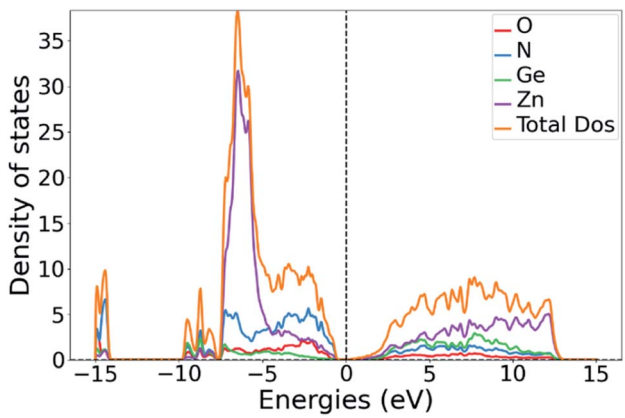

Fig. 6 Total DOS of $Zn_{1.25}Ge_{0.75}(N_{0.75}O_{0.25})_2$ (b) with the partial DOS contributions for the constituent elements.

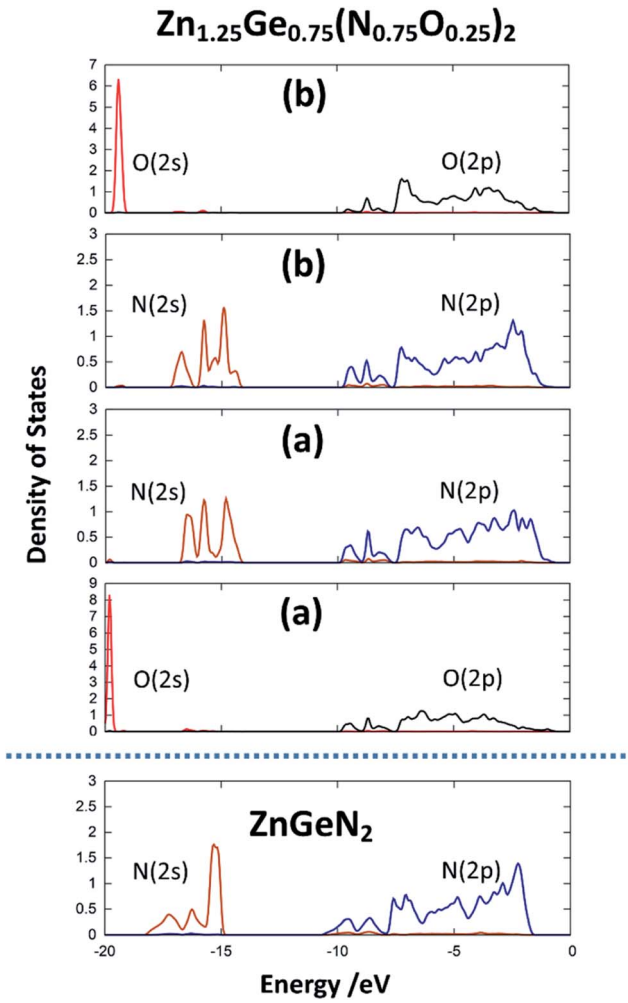

Fig. 7 pDOS for the 2s and 2p orbitals for one selected nitrogen and oxygen atom in the crystal structures for $ZnGeN_2$ and the two configurations of $Zn_{1.25}Ge_{0.75}(N_{0.75}O_{0.25})_2$, as depicted in Fig. 2.

between the band onsets, *i.e.*, the highest energy levels between N(2s) and N(2p) are $\Delta E(ZnGeN_2) = 13.26$ eV *versus* $\Delta E(Zn_{1.25}Ge_{0.75}(N_{0.75}O_{0.25})_2) = 13.52$ eV for (a) and 13.62 eV for (b). This is a clear indication of the fact that the VBM is shifted to higher energies, explaining the reduction of the band gap energy in the oxide nitride materials. It is noteworthy that the oxygen 2p levels lie in the same range and also contribute to the upper valence band, while the O(2s) levels lie significantly lower than the respective N(2s) levels. The energetic levels of the Zn(3d) states show a narrow distribution and are close to the N(2p) and O(2p) states. This is a prerequisite for the orbital overlap that leads to p–d repulsion. We note that the Ge(3d) states are significantly lower – at −25 eV relative to the band gap – and hence are even lower than the N(2s) and O(2s) states. This prevents orbital overlap including these Ge(3d) states and p–d-repulsion is therefore exclusive to Zn

containing bonding. However, one would expect p–d repulsion both for nitrides and oxide nitrides and it is hence important to look at the individual bonding contributions to understand why the upwards shift of the VBM in the latter is stronger than for pure $ZnGeN_2$.

Bonding situation analysis

DOS and pDOS allow a detailed discussion of the atomic distribution to energy states around the band gap, but they contain little information on the nature of the chemical bonds between atoms. For this, we employ crystal orbital overlap Hamilton population (COHP)[68,69] analysis to rationalise the energetic contribution of the chemical bonds and reveal the character of the contributions as bonding or antibonding. Projecting the COHP on individual bonds (pCOHP) allows us to draw direct conclusions for individual bonds. By convention, we plot −COHP with antibonding states on the left and bonding states on the right-hand side of the plot.

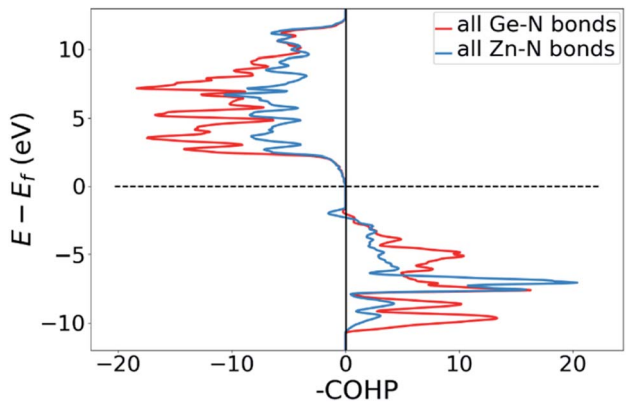

Fig. 8 COHP plot of the summed Zn–N and Ge–N bonds in $ZnGeN_2$.

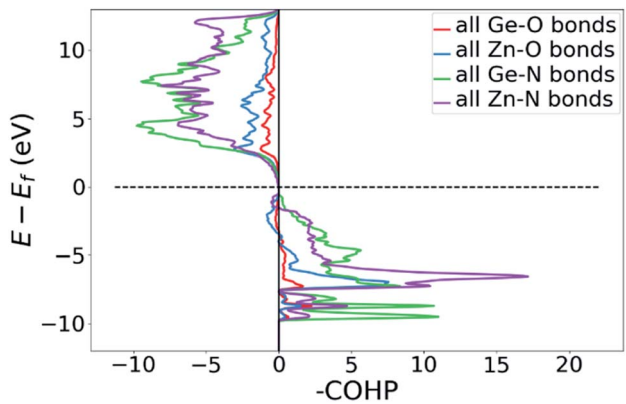

Fig. 9 COHP plot of the summed Zn–N, Ge–N, Zn–O and Ge–O bonds in $Zn_{1.25}Ge_{0.75}(N_{0.75}O_{0.25})_2$ (b).

The populated energy levels of the Ge–N bonds in $ZnGeN_2$ all have a bonding character stabilising the crystal structure (Fig. 8). This is in line with the fact that those bonds are formed by the Ge(4p) orbitals and the N(2p) orbitals and hence would not be prone to p–d-repulsion. In contrast, the COHP of the Zn–N interactions clearly shows antibonding behaviour at the VBM, in line with the p–d repulsion model. The trend in the oxygen containing crystal structures is similar (Fig. 9), with Ge–N bonds still being bonding throughout the valence band. The antibonding contribution of the Zn–N bonds is accompanied by antibonding contributions from the Zn–O and Ge–O bonds. It is, however, noteworthy that the Zn–O antibonding states lie energetically below the antibonding Zn–N states, which suggests that the orbital splitting caused by p–d repulsion is smaller, since the positions of the O(2p) and N(2p) orbitals are otherwise very similar (Fig. 7). Therefore, oxygen does not directly cause the upshift of the valence band maximum but has an indirect effect. Given that Zn–O bond lengths are shorter than Zn–N bond lengths, the geometry of the coordination environment around Zn that contains both anion types is strongly distorted from an ideal tetrahedron, causing non-ideal bonding distances and angles. This, in turn, can affect the energy levels of the Zn–N bonds, causing an upwards shift of the energy levels involved.

Materials and methods

The experimental data was extracted from previous work. Details of the synthesis and characterisation can be found elsewhere.[51,53,55] The "universal" bond valence parameters derived by Brese and O'Keeffe were used for the calculations herein.[66]

DFT calculations were performed using Quantum Espresso v6.5[70–72] with the projector augmented wave (PAW) method[73,74] using GGA functionals with scalar-relativistic PBE-type exchange–correlation functionals with non-linear core correction.[75,76] The pseudopotentials were retrieved from pslibrary[77] and produced using atomic.[78] The wavefunction cutoff was chosen to be 50 Ry and the charge density cutoff was chosen to be 325 Ry. Structural optimisations were performed using a $3 \times 3 \times 3$ *k*-point grid and a BFGS algorithm. The unit cell was constrained during optimisation to remain orthonormal.

SCF calculations for DOS and COHP calculations were performed on a $12 \times 12 \times 12$ *k*-point grid and an energy convergence threshold of 10^{-9}. In order to permit the density partitioning, 104 bands were converged during the SCF calculation, reflecting the 104 orbitals used for portioning ($8 \times$ N/O($2s2p_xp_yp_z$) + $8 \times$ Zn/Ge($4s4p_xp_yp_z3d_{xy}d_{xz}d_{yz}d_{z^2}d_{x^2-y^2}$)).

DOS and COHP calculations were performed using LOBSTER 4.1.0 (ref. 79 and 80) with a Gaussian smearing width of 0.1 eV with the pbeVaspFit2015 basis set.[79] COHP and DOS plots were obtained using pymatgen.[81]

Conclusions

The incorporation of oxygen in the crystal structure of zinc germanium oxide nitrides leads to a narrowing of the band gap. We have explored the structural consequences of the introduction of oxygen in this system to uncover which effects it has and this can be decorrelated from the intrinsic disorder. While experimental samples with high oxygen content also show a high degree of

intrinsic disorder, oxygen incorporation alone was studied using DFT calculations. The latter still shows significant deviation of the lattice constants from the hexagonal wurtzite type, while experimental compounds with a similar compositions show unit cell parameters much closer to the hexagonal lattice constants. Therefore, it is concluded that the interplay of intrinsic and extrinsic disorder causes this behaviour, rather than one mechanism alone. Using DOS and COHP analyses, we have further shown that the narrowing of the band gap in oxide nitride materials is caused by increasing the p–d repulsion effect as a consequence of deviating from the coordination environments of Zn.

Author contributions

J. B. designed the study, conducted the calculations and did the initial data treatment. Su. S. and J. B. discussed the results and J. B. wrote the manuscript with input from Su. S.

Conflicts of interest

There are no conflicts to declare.

Acknowledgements

The authors acknowledge Zhenyu Wang for the synthesis and analysis of the experimental data.

Notes and references

1 *Solar is now 'cheapest electricity in history', confirms IEA*, **https://www.carbonbrief.org/solar-is-now-cheapest-electricity-in-history-confirms-iea**, accessed February 6, 2022.
2 R. M. Geisthardt, M. Topic and J. R. Sites, *IEEE J. Photovolt.*, 2015, **5**, 1217–1221.
3 M. Gloeckler, I. Sankin and Z. Zhao, *IEEE J. Photovolt.*, 2013, **3**, 1389–1393.
4 C. S. Ferekides, D. Marinskiy, V. Viswanathan, B. Tetali, V. Palekis, P. Selvaraj and D. L. Morel, *Thin Solid Films*, 2000, **361–362**, 520–526.
5 A. Romeo, M. Terheggen, D. Abou-Ras, D. L. Bätzner, F.-J. Haug, M. Kälin, D. Rudmann and A. N. Tiwari, *Prog. Photovoltaics Res. Appl.*, 2004, **12**, 93–111.
6 V. D. Novruzov, N. M. Fathi, O. Gorur, M. Tomakin, A. I. Bayramov, S. Schorr and N. Mamedov, *Phys. Status Solidi A*, 2010, **207**, 730–733.
7 L. Kranz, S. Buecheler and A. N. Tiwari, *Sol. Energy Mater. Sol. Cells*, 2013, **119**, 278–280.
8 X. Cai, S. Zeng and B. Zhang, *Appl. Phys. Lett.*, 2009, **95**, 173504.
9 R. Dahal, B. Pantha, J. Li, J. Y. Lin and H. X. Jiang, *Appl. Phys. Lett.*, 2009, **94**, 063505.
10 R.-H. Horng, S.-T. Lin, Y.-L. Tsai, M.-T. Chu, W.-Y. Liao, M.-H. Wu, R.-M. Lin and Y.-C. Lu, *IEEE Electron Device Lett.*, 2009, **30**, 724–726.
11 O. Jani, I. Ferguson, C. Honsberg and S. Kurtz, *Appl. Phys. Lett.*, 2007, **91**, 132117.
12 T. Takamoto, E. Ikeda, H. Kurita and M. Ohmori, *Appl. Phys. Lett.*, 1997, **70**, 381–383.

13 T. Takamoto, E. Ikeda, H. Kurita and M. Ohmori, in *Proceedings of 1994 IEEE 1st World Conference on Photovoltaic Energy Conversion – WCPEC (A Joint Conference of PVSC, PVSEC and PSEC)*, 1994, vol. 2, pp. 1729–1732.
14 T. Takamoto, M. Kaneiwa, M. Imaizumi and M. Yamaguchi, *Prog. Photovoltaics Res. Appl.*, 2005, **13**, 495–511.
15 N. J. Ekins-Daukes, K. W. J. Barnham, J. P. Connolly, J. S. Roberts, J. C. Clark, G. Hill and M. Mazzer, *Appl. Phys. Lett.*, 1999, **75**, 4195–4197.
16 N. Dharmarasu, M. Yamaguchi, A. Khan, T. Yamada, T. Tanabe, S. Takagishi, T. Takamoto, T. Ohshima, H. Itoh, M. Imaizumi and S. Matsuda, *Appl. Phys. Lett.*, 2001, **79**, 2399–2401.
17 J. M. Zahler, K. Tanabe, C. Ladous, T. Pinnington, F. D. Newman and H. A. Atwater, *Appl. Phys. Lett.*, 2007, **91**, 012108.
18 C. Candelise, M. Winskel and R. Gross, *Prog. Photovoltaics Res. Appl.*, 2012, **20**, 816–831.
19 Y.-C. Wang, T.-T. Wu and Y.-L. Chueh, *Mater. Chem. Phys.*, 2019, **234**, 329–344.
20 Y. Zhao, S. Yuan, D. Kou, Z. Zhou, X. Wang, H. Xiao, Y. Deng, C. Cui, Q. Chang and S. Wu, *ACS Appl. Mater. Interfaces*, 2020, **12**, 12717–12726.
21 M. Theelen and F. Daume, *Sol. Energy*, 2016, **133**, 586–627.
22 G. Hodes, *Science*, 2013, **342**, 317–318.
23 M. A. Green, A. Ho-Baillie and H. J. Snaith, *Nat. Photonics*, 2014, **8**, 506–514.
24 A.-F. Castro-Méndez, J. Hidalgo and J.-P. Correa-Baena, *Adv. Energy Mater.*, 2019, **9**, 1901489.
25 G. Hodes and D. Cahen, *Nat. Photonics*, 2014, **8**, 87–88.
26 A. A. Yaroshevsky, *Geochem. Int.*, 2006, **44**, 48–55.
27 *Directive 2011/65/EU of the European Parliament and of the Council of 8 June 2011 on the restriction of the use of certain hazardous substances in electrical and electronic equipment Text with EEA relevance*, 2011, vol. 174.
28 F. Giustino and H. J. Snaith, *ACS Energy Lett.*, 2016, **1**, 1233–1240.
29 A. Abate, *Joule*, 2017, **1**, 659–664.
30 L. Liang and P. Gao, *Adv. Sci.*, 2018, **5**, 1700331.
31 D. Ramirez, F. Jaramillo, S. Pérez-Walton and J. M. Osorio-Guillén, *J. Chem. Phys.*, 2018, **148**, 244703.
32 J. Breternitz, S. Levcenko, H. Hempel, G. Gurieva, A. Franz, A. Hoser and S. Schorr, *JPhys Energy*, 2019, **1**, 025003.
33 N. Feldberg, B. Keen, J. D. Aldous, D. O. Scanlon, P. A. Stampe, R. J. Kennedy, R. J. Reeves, T. D. Veal and S. M. Durbin, in *2012 38th IEEE Photovoltaic Specialists Conference*, IEEE, 2012.
34 S. Nakatsuka, N. Yuzawa, J. Chantana, T. Minemoto and Y. Nose, *Phys. Status Solidi A*, 2017, **214**, 1600650.
35 K. Javaid, J. Yu, W. Wu, J. Wang, H. Zhang, J. Gao, F. Zhuge, L. Liang and H. Cao, *Phys. Status Solidi RRL*, 2018, **12**, 1700332.
36 I. S. Khan, K. N. Heinselman and A. Zakutayev, *J. Phys. Energy*, 2020, **2**, 032007.
37 K. Javaid, W. Wu, J. Wang, J. Fang, H. Zhang, J. Gao, F. Zhuge, L. Liang and H. Cao, *ACS Photonics*, 2018, **5**, 2094–2099.
38 R. Qin, H. Cao, L. Liang, Y. Xie, F. Zhuge, H. Zhang, J. Gao, K. Javaid, C. Liu and W. Sun, *Appl. Phys. Lett.*, 2016, **108**, 142104.
39 X. Cao, F. Kawamura, Y. Ninomiya, T. Taniguchi and N. Yamada, *Sci. Rep.*, 2017, **7**, 14987.
40 X. Cao, F. Kawamura, T. Taniguchi and N. Yamada, *BMC Mater.*, 2020, **2**, 4.

41 M. S. Haseman, M. R. Karim, D. Ramdin, B. A. Noesges, E. Feinberg, B. H. D. Jayatunga, W. R. L. Lambrecht, M. Zhu, J. Hwang, K. Kash, H. Zhao and L. J. Brillson, *J. Appl. Phys.*, 2020, **127**, 135703.
42 A. L. Greenaway, C. L. Melamed, M. B. Tellekamp, R. Woods-Robinson, E. S. Toberer, J. R. Neilson and A. C. Tamboli, *Annu. Rev. Mater. Res.*, 2021, **51**, 591–618.
43 C. L. Melamed, M. B. Tellekamp, J. S. Mangum, J. D. Perkins, P. Dippo, E. S. Toberer and A. C. Tamboli, *Phys. Rev. Mater.*, 2019, **3**, 051602.
44 W. Sun, C. J. Bartel, E. Arca, S. R. Bauers, B. Matthews, B. Orvañanos, B.-R. Chen, M. F. Toney, L. T. Schelhas, W. Tumas, J. Tate, A. Zakutayev, S. Lany, A. M. Holder and G. Ceder, *Nat. Mater.*, 2019, **18**, 732–739.
45 Y. Lee, H. Terashima, Y. Shimodaira, K. Teramura, M. Hara, H. Kobayashi, K. Domen and M. Yashima, *J. Phys. Chem. C*, 2007, **111**, 1042–1048.
46 K. Maeda and K. Domen, *MRS Bull.*, 2011, **36**, 25–31.
47 Y. Lee, K. Teramura, M. Hara and K. Domen, *Chem. Mater.*, 2007, **19**, 2120–2127.
48 K. Takanabe, T. Uzawa, X. Wang, K. Maeda, M. Katayama, J. Kubota, A. Kudo and K. Domen, *Dalton Trans.*, 2009, 10055–10062.
49 F. Tessier, P. Maillard, Y. Lee, C. Bleugat and K. Domen, *J. Phys. Chem. C*, 2009, **113**, 8526–8531.
50 X. Wang, K. Maeda, Y. Lee and K. Domen, *Chem. Phys. Lett.*, 2008, **457**, 134–136.
51 Z. Y. Wang, D. Fritsch, S. Berendts, M. Lerch, J. Breternitz and S. Schorr, *Chem. Sci.*, 2021, **12**, 8493–8500.
52 P. Bacher, G. Roult, M. Ghers, O. Merdrignac, J. Guyader and Y. Laurent, *Mater. Chem. Phys.*, 1989, **21**, 223–235.
53 J. Breternitz, Z. Y. Wang, A. Franz, S. Savvin, D. M. Többens and S. Schorr, in preparation.
54 S.-H. Wei and A. Zunger, *Phys. Rev. B: Condens. Matter Mater. Phys.*, 1988, **37**, 8958–8981; S.-H. Wei and A. Zunger, *J. Appl. Phys.*, 1995, **78**, 3846–3856.
55 J. Breternitz, Z. Y. Wang, A. Glibo, A. Franz, M. Tovar, S. Berendts, M. Lerch and S. Schorr, *Phys. Status Solidi A*, 2019, **216**, 1800885.
56 M. Wintenberger, M. Maunaye and Y. Laurent, *Mater. Res. Bull.*, 1973, **8**, 1049–1053.
57 W. L. Larson, H. P. Maruska and D. A. Stevenson, *J. Electrochem. Soc.*, 1974, **121**, 1673.
58 R. D. Shannon, *Acta Crystallogr., Sect. A*, 1976, **32**, 751–767.
59 J. Breternitz and S. Schorr, *Acta Crystallogr., Sect. A*, 2021, **77**, 208–216.
60 Creative Commons — Attribution 3.0 Unported — CC BY 3.0, **https://creativecommons.org/licenses/by/3.0/**, accessed February 4, 2022.
61 J. J. Cordell, J. Pan, A. C. Tamboli, G. J. Tucker and S. Lany, *Phys. Rev. Mater.*, 2021, **5**, 024604.
62 D. Skachkov, P. C. Quayle, K. Kash and W. R. L. Lambrecht, *Phys. Rev. B*, 2016, **94**, 205201.
63 C. L. Melamed, J. Pan, A. Mis, K. Heinselman, R. R. Schnepf, R. Woods-Robinson, J. J. Cordell, S. Lany, E. S. Toberer and A. C. Tamboli, *J. Mater. Chem. C*, 2020, **8**, 8736–8746.
64 I. D. Brown, *Acta Crystallogr., Sect. B: Struct. Crystallogr. Cryst. Chem.*, 1977, **33**, 1305–1310.

65 M. O'Keefe and N. E. Brese, *J. Am. Chem. Soc.*, 1991, **113**, 3226–3229.
66 N. E. Brese and M. O'Keeffe, *Acta Crystallogr., Sect. B: Struct. Crystallogr. Cryst. Chem.*, 1991, **47**, 192–197.
67 I. D. Brown, *Chem. Rev.*, 2009, **109**, 6858–6919.
68 R. Dronskowski and P. E. Bloechl, *J. Phys. Chem.*, 1993, **97**, 8617–8624.
69 V. L. Deringer, A. L. Tchougréeff and R. Dronskowski, *J. Phys. Chem. A*, 2011, **115**, 5461–5466.
70 S. Scandolo, P. Giannozzi, C. Cavazzoni, S. de Gironcoli, A. Pasquarello and S. Baroni, *Z. Kristallogr. – Cryst. Mater.*, 2005, **220**, 574–579.
71 P. Giannozzi, S. Baroni, N. Bonini, M. Calandra, R. Car, C. Cavazzoni, D. Ceresoli, G. L. Chiarotti, M. Cococcioni, I. Dabo, A. D. Corso, S. de Gironcoli, S. Fabris, G. Fratesi, R. Gebauer, U. Gerstmann, C. Gougoussis, A. Kokalj, M. Lazzeri, L. Martin-Samos, N. Marzari, F. Mauri, R. Mazzarello, S. Paolini, A. Pasquarello, L. Paulatto, C. Sbraccia, S. Scandolo, G. Sclauzero, A. P. Seitsonen, A. Smogunov, P. Umari and R. M. Wentzcovitch, *J. Phys.: Condens. Matter*, 2009, **21**, 395502.
72 P. Giannozzi, O. Andreussi, T. Brumme, O. Bunau, M. B. Nardelli, M. Calandra, R. Car, C. Cavazzoni, D. Ceresoli, M. Cococcioni, N. Colonna, I. Carnimeo, A. D. Corso, S. de Gironcoli, P. Delugas, R. A. DiStasio, A. Ferretti, A. Floris, G. Fratesi, G. Fugallo, R. Gebauer, U. Gerstmann, F. Giustino, T. Gorni, J. Jia, M. Kawamura, H.-Y. Ko, A. Kokalj, E. Küçükbenli, M. Lazzeri, M. Marsili, N. Marzari, F. Mauri, N. L. Nguyen, H.-V. Nguyen, A. Otero-de-la-Roza, L. Paulatto, S. Poncé, D. Rocca, R. Sabatini, B. Santra, M. Schlipf, A. P. Seitsonen, A. Smogunov, I. Timrov, T. Thonhauser, P. Umari, N. Vast, X. Wu and S. Baroni, *J. Phys.: Condens. Matter*, 2017, **29**, 465901.
73 P. E. Blöchl, *Phys. Rev. B: Condens. Matter Mater. Phys.*, 1994, **50**, 17953–17979.
74 G. Kresse and D. Joubert, *Phys. Rev. B: Condens. Matter Mater. Phys.*, 1999, **59**, 1758–1775.
75 J. P. Perdew, K. Burke and M. Ernzerhof, *Phys. Rev. Lett.*, 1996, **77**, 3865–3868.
76 J. P. Perdew, K. Burke and M. Ernzerhof, *Phys. Rev. Lett.*, 1997, **78**, 1396.
77 *Pseudo search results – QUANTUMESPRESSO*, **http://pseudopotentials.quantum-espresso.org/legacy_tables/ps-library/zn**, accessed February 6, 2022.
78 A. Dal Corso, *Comput. Mater. Sci.*, 2014, **95**, 337–350.
79 S. Maintz, V. L. Deringer, A. L. Tchougréeff and R. Dronskowski, *J. Comput. Chem.*, 2016, **37**, 1030–1035.
80 R. Nelson, C. Ertural, J. George, V. L. Deringer, G. Hautier and R. Dronskowski, *J. Comput. Chem.*, 2020, **41**, 1931–1940.
81 S. P. Ong, W. D. Richards, A. Jain, G. Hautier, M. Kocher, S. Cholia, D. Gunter, V. L. Chevrier, K. A. Persson and G. Ceder, *Comput. Mater. Sci.*, 2013, **68**, 314–319.

